Integrated Ray Tracing simulation of the SCOTS surface measurement test for the GMT Fast Steering Mirror Prototype

Ji Nyeong Choi [a], Dongok Ryu [a], Sug-Whan Kim [a,b,*], Dae Wook Kim [c], Peng Su [c], Run Huang [c], Young-Soo Kim [d], Ho-Soon Yang [e]

[a] *Space Optics Laboratory, Dept. of Astronomy, Yonsei University, Seoul 120-749, Korea*
[b] *Center for Galaxy Evolution Research, Yonsei University, Seoul 120-749, Korea*
[c] *College of Optical Sciences, the University of Arizona, Tucson, AZ 85721, USA*
[d] *Korea Astronomy and Space Science Institute, Daejeon 305-348, Korea*
[e] *Korea Research Institute of Standards and Science, Daejeon 305-340, Korea*

Abstract

Software Configurable Optical Testing System (SCOTS) is one of relatively new optical testing methods for large optical surfaces and uses the principle of Phase Measuring Deflectometry (PMD). A camera captures images of the target surface illuminated by a light source screen with patterns. Then, the surface slope and height are obtained by camera image analysis. In the meantime, Integrated Ray Tracing (IRT) concept was developed for the simultaneous end-to-end imaging and radiometric performance simulation of space instruments. It incorporates a light source, medium, target and observing instrument into single computation environment for real scale ray tracing. In this study, we combined these two techniques for the development of an optical testing simulation model applicable to testing the secondary mirror (M2) of Giant Magellan Telescope (GMT). Using the IRT SCOTS model, we simulated SCOTS test runs and reconstructed its surface slopes and heights from the simulated image data. The result shows 1.05 nm rms in difference between the input and reconstructed surface heights. It demonstrates the high fidelity of the suggested IRT approach showing nanometer level numerical accuracy and therefore it shows the potential applicability of the IRT simulation technique to SCOTS test method for large precision optical surfaces.

© 2015 COSPAR. Published by Elsevier Ltd. All rights reserved.

Keywords: Telescope; Optical testing; Deflectometry; Integrated Ray Tracing

1. Introduction

Today, 1 m class large aspheric mirrors are favorite choices for the segmented primary and secondary mirrors of state-of-the-art ground based and space based large telescopes. Examples are listed in Table 1. It is well known that fabrication of such mirrors are challenging because of (1) surface precision down to nanometer scales and (2) large

departures from spherical surfaces i.e. asphericity. Such examples may include, but not limited to Giant Magellan Telescope Fast Steering Mirror (GMT FSM), the backup secondary mirror assembly of GMT, and its characteristics are listed in Table 2 (Kim et al., 2012; Cho et al., 2014). The GMT secondary mirror (M2) has 7 segments. The M2 mirror at the center is an on-axis aspheric mirror whilst the remaining 6 M2 mirrors are off-axis aspheric surfaces. The individual segments of FSM have 3.1 mm in peak to valley aspheric departures, implying its fabrication and testing difficulty.

Table 1
Examples of 1 m class mirrors for space and ground telescopes and their surface test method.

Telescope	Dia. (m)	Curv. radi. (mm)	Conic constant	Test method (measured rms error)	Reference
E-ELT (PM[1])	1.45	∼84000	−0.9933	CMM (2.0 ± 0.3 μm) CGH (23 ± 8 nm)	Comley et al. (2011), Rodolfo et al. (2012)
JWST (PM[1])	1.52	15899.9	−0.9967	CMM(19 ± 3 μm) SSHS[3] (19 ± 1 μm) CGH (15.4 ± 2.5 nm)	Kiikka et al. (2006), Gallagher et al. (2011)
VISTA (SM[1,2])	1.24	4018.9	−5.5488	Hindle sphere Interferometry (66 ± 30 nm)	Abdulkadyrov et al. (2004)
LBT (SM[1,2])	0.91	1974.0	−0.7328	Swing arm profilometer (∼50 ± 10 nm) Null lens Interferometry (∼10 ± 1 nm)	Martin et al. (2006)

[1] PM (primary mirror) and SM (secondary mirror).
[2] Convex mirror.
[3] Scanning Shack Hartmann System.

Table 2
GMT FSM surface specification.

Item	Value	Remarks
Diameter	3.2 m (7 segments total)	1.064 m for each segment
Radius of curvature	4166.747 mm	Concave
Conic constant	−0.7154	Ellipsoid
F-number (F/#)	0.65	

Optical testing is a key process step for such mirror fabrication as it provides opticians with the mirror surface data to be corrected in successive machine runs. Several testing methods have been developed over the last few decades. They include Coordinate Measuring Machine (CMM), profilometry, interferometric null lens testing and Computer Generated Hologram (CGH) interferometric testing (Valente et al., 2013). Whilst these methods have been successfully used for the large optics fabrication process, they tend to suffer from (1) high cost of the measurement equipment, (2) limited spatial resolution and measurement accuracy from CMM and profilometry, (3) alignment precision of the interferometer, (4) high cost together with unpredictable delivery of customized null lens and CGH, and finally (5) interpretation difficulty of fringe data from null lens testing and CGH testing (Kim et al., 2009). These give rise to the importance of developing a new low cost yet high precision optical testing apparatus for efficient fabrication process of aforementioned 1 m class mirrors.

In the meantime, the principle of Phase Measuring Deflectometry (PMD) (Knauer et al., 2004) has been developed using the moiré interferometry (Ligtenberg, 1954). Its apparatus consists of a camera, an illuminating screen and surface reconstruction computation engine. The camera is to capture the target mirror image illuminated by the light from the light source screen with sinusoidal fringe pattern. It offers good potentials to construction of the low cost large optics testing equipment achieving large measurement dynamic range and high accuracy when aided by the precise calibration. Software Configurable Optical Test System (SCOTS) is one of such PMD tests and has been applied for various astronomical optics including 8.4 m GMT primary off-axis segment at the University of Arizona and the results showed its accuracy comparable to nanometer scale (Su et al., 2010, 2012a,b). It implies that PMD type measurement equipment, for example SCOTS, can be an interesting alternative to both CMM and interferometric measurements for testing large optical surfaces.

However, we note that SCOTS measurement accuracy relies heavily on the calibration quality of the instrument used and there are several elements that tent to influence the calibration quality and hence the final surface measurement accuracy. Examples may include, but not limited to, the relative positions of the screen, target mirror and camera, camera aberration, diffraction within the optical train, scattered light noise, and so on. Whilst the PMD and SCOTS measurement concept, and the instrument set up are all simple and cost-effective, the actual measurement run and the preparation before and during the shop floor measurement are laborious and time consuming.

The theoretical background and hence the analytical model of SCOTS use reverse ray tracing technique from the detector to the illuminating screen and it is combined with PSF convolution method (Su et al., 2015). And typical SCOTS experiment uncertainties involved in the measurement are briefly summarized in Table 1 of the study from Su et al. (2012c). We note that the SCOTS technique deals a wide range of error sources with actual experimental data obtained prior to the mirror test run and no analysis model was built to investigate their characteristics of the error sources properly and in details. This is because the aforementioned SCOTS analytical model using sequential ray tracing and PSF convolution is incapable of analyzing the error sources categorized as 'ignorable' in Table 1 from Su et al. (2012c).

In particular, error sources such as light intensity angular effect, ghost imaging, scatter light and etc. were not numerically analyzed and yet claimed to cause ignorable effects to the measurement. We understand that such error sources can be analyzed effectively by using a

non-sequential ray tracing technique capable of computing transfer of radiometric power from the illuminating screen to the detector pixels. The uncertainties from those error sources can be quantitatively estimated with the new technique before building actual SCOTS hardware. As a result, some of the errors doesn't need to be calibrated as long as their uncertainty contributions are within allowable error budget. This would greatly reduce the calibration efforts including time and cost. The suggested non-sequential forward ray tracing technique would also provide the SCOTS users with the test mirror image overlapped with the illuminated and distorted fringe pattern that is the only observed phenomena from the experiment. The existing SCOTS analysis tool (Su et al., 2015) is incapable of delivering such observed phenomena to the SCOTS user for further investigation before, during and after the measurement.

In the meantime, Integrated Ray Tracing (IRT) technique has been developed for the end-to-end performance simulation of space instruments (Jeong et al., 2009; Ryu et al., 2010) over the last few years. The technique offers unique computational capability of both imaging and radiometric performance for an optical instrument as it traces the light rays non-sequentially from the source to the final instrument detector plane. Several studies on the proposed AmonRa earth albedo measurement instrument have been made successfully over the last few years (Lee et al., 2007; Seong et al., 2012).

In this study, we combine the IRT technique with the aforementioned SCOTS method and a new SCOTS IRT model is reported for the first time. And then it is applied to the GMT FSM measurement simulation for its computation performance investigation. In Section 2, the concepts of SCOTS and IRT SCOTS model are described. The simulation cases and results are reported in Section 3. This is followed by the discussions on the factors influencing simulation errors in Section 4, before the concluding remarks in Section 5.

2. IRT model for SCOTS image simulation

2.1. IRT SCOTS model

The SCOTS test can be considered as a reverse Hartmann test (Su et al., 2010). Each pixel on the detector has one to one correspondence to each sampling point on the target surface. Fig. 1(a) shows the schematic diagram of SCOTS geometric test configuration. The screen and pinhole camera are located near to the center of curvature of the target surface and this tends to loosen its alignment tolerance (Su et al., 2014). The scanning line or sinusoidal pattern are illuminated onto the target surface and the camera captures the test surface images formed by reflected light rays from the target surface.

The first target surface used in the IRT SCOTS model is a spherical surface of 1064.00 mm in diameter and 4166.747 mm in radius of curvature and these are same as those of GMT FSM (Table 2). In order to represent realistic optical surface errors, we generated yet another hypothetical target surface as well. It is spherical surface with 0.4828 μm rms in deviation from the target surface and it is derived from using Zernike polynomial terms as listed in Table 3. The surface deviation scale is only about 1/50,000 of the target surface height. These spherical and

Table 3
Input Zernike polynomial terms and coefficient for surface deviation.

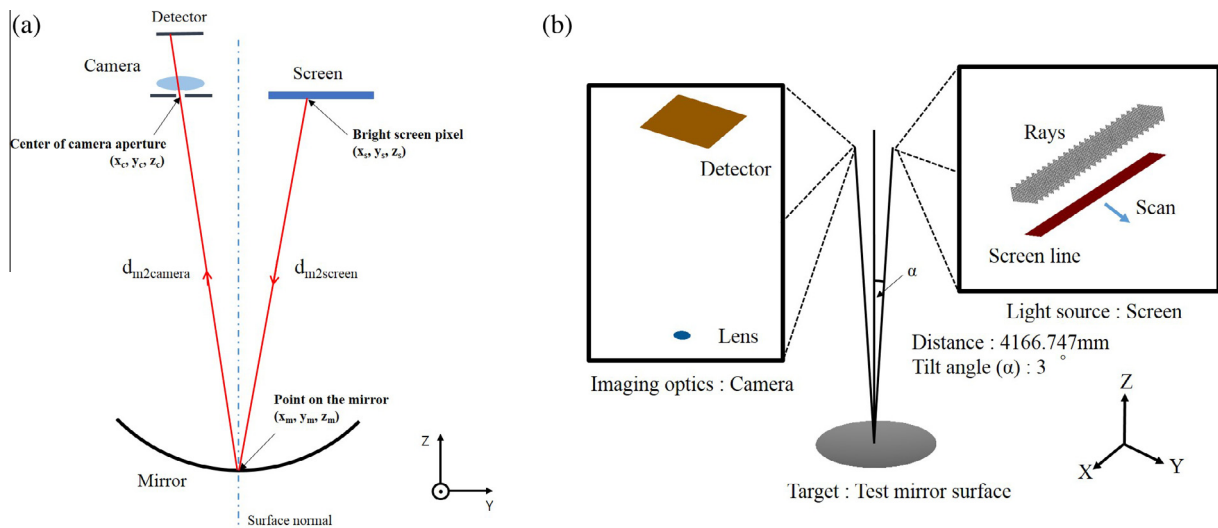| Zernike term (order)	Input coefficient (μm)
Primary Astigmatism x (6)	0.3266
Primary Coma x (8)	−0.1414
Primary Trifoil y (9)	0.1061
Primary Spherical (11)	0.0894
Tertiary Coma x (29)	−0.0250
Quaterary Astig y (38)	-0.0141
RMS surface deviation (μm)	0.4828

Fig. 1. (a) Is a schematic diagram of SCOTS surface test. (b) Shows the SCOTS geometric modeling in IRT simulation.

deviated spherical surfaces are placed in XY plane and their reflecting surfaces are looking upward in $+Z$ direction as in Fig. 1(b). The ray tracing simulation was performed for both the ideal spherical surface and the deviated surfaces. The results are then compared against each other. We used Breault Research Organization's Advanced Systems Analysis Program, ASAP® for real scale non-sequential forward ray tracing.

The SCOTS IRT model has an illuminating screen and a camera placed at about 4166.747 mm in $+Z$ distance from the center of the target surface. The distance is same as the radius of curvature of the target spherical surface. They are tilted about ± 3 degrees from the $+Z$ axis as illustrated in Fig. 1(b). The 3 degrees tilted angle was decided by two factors, (1) distance from the target surface to the SCOTS and (2) distance between the camera and the screen, in order to physically separate the camera and screen. We used a paraxial singlet as the detecting camera to ignore the camera aberrations and wavefront errors and to focus on the effect of the different test surface wavefront between the input and distorted surfaces. The camera aperture is defined as 1 mm in diameter and the focal length is 16 mm. The detector plane is located at around 16 mm in $+Z$ distance from the paraxial lens and consists of 125 by 125 pixels of 37 μm in pitch size. The 37 μm pitch size, which simulates a binned pixel case (i.e. 8 detector pixels of 4.65 μm in pitch size), was used in order to increase the numerical simulation accuracy (for a fixed total ray number) at the cost of lower spatial resolution in the final surface map. We used reverse ray tracing from the detector pixels to the mirror in order to obtain the camera calibration data that is subsequently used for compensation of the mirror position corresponding to each detector pixel.

The screen model is defined as a Lambertian scattering plane. The screen pixel pitch size is 200 μm in length and 21 by 21 screen pixels are used to form the target image. The line scanning method (Su et al., 2010) was used when illuminating the screen pattern to the target surface. The line is defined as a set of screen pixels making line shape in the direction of x and y axis. 21 lines were created in a scan direction and 21 images for each X and Y scan

direction were obtained. Rays are expression of the emitting light from screen pixel. In Fig. 1(b), rays are generated from the back of screen plane. When ray tracing begins, the rays strike the screen plane and illuminating rays are generated on the line's screen pixels. Fig. 2(a) shows the IRT model of screen with the illuminating rays. In terms of traced ray numbers, three study cases (i.e. 156,250, 1,562,500 and 15,625,000 rays per screen pixel) were used based on the preliminary trade-off study between the computation time and the accuracy of the re-constructed surface wavefront.

In ray tracing computation, the traveling direction of light ray is computed from using Snell's law and Fresnel equation. In doing so, the radiant power of each ray arriving at the detector (f_d) is computed by successive use of Eq. (1) as they encounter with each optical surface (Breault et al., 2014). f_i is radiant power of the incident ray before scattering takes place at the screen. The angle of incident ray before the screen is set as constant and the screen is a transmitting layer with Lambertian scattering characteristics. Therefore the screen Bidirectional Scattering Distribution Function (BSDF) is constant over all scattering angles. R_{mirror} is the reflectivity of mirror surface and T_{optics} is transmittance of the camera lens. In general the reflective coating provides the mirror with 98% in reflectance and the surface scattering would follow Davies' scattering law with a range of 0.01–0.05% in Total Integrated Scatter (TIS) (Davies, 1954). Thus it is reasonable to assume that the target mirror and camera lens surfaces have negligible scattering for this ray tracing computation.

$$f_d = f_i \cdot \text{BSDF}(\theta_s, \varphi_s) \cdot R_{mirror} \cdot T_{optics} \qquad (1)$$

As shown in Fig. 2, only limited number of light ray reach to the detector plane as the camera aperture, through which the light rays pass, is only 1 mm in diameter. If the arriving ray number at the detector is too small, they tend to cause fluctuation of irradiance distribution across the detector plane. Thus, we needed over millions of light rays emitted from the screen so that the numerical simulation accuracy is improved, as discussed later in Section 4.
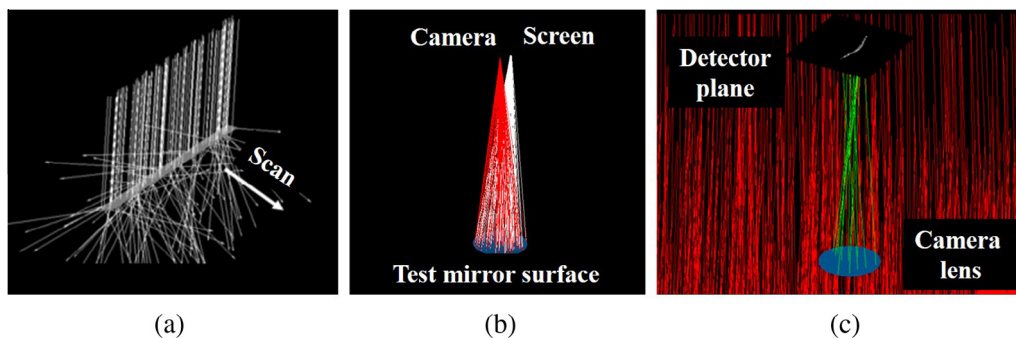

(a)   (b)   (c)

Fig. 2. IRT process. (a) Is simulation of screen pixel illumination as light source. (b) Shows reflection from the test surface. (c) Shows rays entering into the camera module and image generation expressed by the green colored rays. For visualization purposes, only 1% of light rays used are presented in these figures.

Eq. (2) is used to compute approximated flux arriving at the detector pixel (Φ) (Su et al., 2013). Here r is reflectance of the target surface and L is radiance of each screen pixel. A_w is the area through which the light passes within the camera aperture and varied with the line position in the screen. Ω_p is the solid angle of corresponding detector pixel, as seen from the center of the camera aperture. As reflectance and radiance, solid angle of the detector pixel are nearly constant, the flux arriving at each pixel is strongly influenced by A_w, this leads to the light curve that is the normalized irradiance received by single pixel as the line pattern moves across the camera aperture.

$$\Phi = r \cdot L \cdot A_w \cdot \Omega_p \tag{2}$$

2.2. Image analysis and surface reconstruction

Similar to the Hartman test, when rays start travelling from the center of the camera aperture, each ray reaches to the target surface, and then reflected toward the screen. It is then obvious that two surface slopes in X and Y axis directions (w_x, w_y) can be computed by using the coordinate of the center of camera aperture, and of the two ono-to-one corresponding points on the test surface and on the screen. The slope can be obtained from using Eq. (3) that uses the principle of the triangulation (Su et al., 2010).

$$w_x(x_m, y_m) = \frac{\frac{x_m - x_{screen}}{d_{m2screen}} + \frac{x_m - x_{camera}}{d_{m2camera}}}{\frac{z_{m2screen} - w(x_m, y_m)}{d_{m2screen}} + \frac{z_{m2camera} - w(x_m, y_m)}{d_{m2camera}}}$$

$$w_y(x_m, y_m) = \frac{\frac{y_m - y_{screen}}{d_{m2screen}} + \frac{y_m - y_{camera}}{d_{m2camera}}}{\frac{z_{m2screen} - w(x_m, y_m)}{d_{m2screen}} + \frac{z_{m2camera} - w(x_m, y_m)}{d_{m2camera}}} \tag{3}$$

Here, x_m and y_m are the coordinates of a point on the test surface; x_{camera} and y_{camera} are coordinates of the center of the camera aperture; x_{screen} and y_{screen} are the coordinates of screen pixel, from which the light ray starts travelling and ends at a given detector pixel; $d_{m2sreen}$ and $d_{m2camera}$ are distances from the test surface point to the screen pixel and to the center of camera aperture respectively; $z_{m2screen}$

and $z_{m2camera}$ are the Z coordinate difference from the test surface to the surface pixel and to the center of camera aperture respectively as well.

Two scan directions of line pattern were used and input to Eq. (4) that is the line centroid equation (Su et al., 2010). We defined the centroid as input parameter of x_{screen} and y_{screen} to Eq. (3). The screen area corresponding to a detector pixel occupies a number of screen pixels and this area is defined as Effective Screen Pixel (ESP). The centroid is defined as the irradiance weighted average position of detector pixels in ESP and Eq. (4) is used to compute the centroid from pixel-to-pixel light curve data. Here x_i and y_i are the coordinate of the ith line position on the screen; I_i is the signal of corresponding detector pixel when the ith line is lit up. Then, two orthogonal directions of the slope are derived from Eq. (3) and then the slope data is converted to the height data by using the zonal estimation technique (Southwell, 1980).

$$x_{screen} = \frac{\sum_{i \in ESP} x_i I_i}{\sum_{i \in ESP} I_i}, \quad y_{screen} = \frac{\sum_{i \in ESP} y_i I_i}{\sum_{i \in ESP} I_i} \tag{4}$$

3. Image simulation and surface reconstruction

3.1. Simulation line scan images

Fig. 3 shows the simulated mirror images under the illumination of the 7th line when scanning the line pattern. The difference in each detector pixel signal is about 6.16% of detector signal on average, only considering overlapping part of images. It is caused by aforementioned 0.4828 µm rms in surface error. Fig. 4 shows the change in image quality as the traced ray number increases. We note that the images become sharper and the irradiance fluctuation decreases from Fig. 4(a –c). For this study, Signal to Noise Ratio (SNR) is defined as a ratio of averaged irradiance at the detector center pixel over 10 simulated mirror images to its standard deviation. It is natural that SNR would increases with the number of ray used. This is proved that the calculated SNR are 3.38, 15.10 and
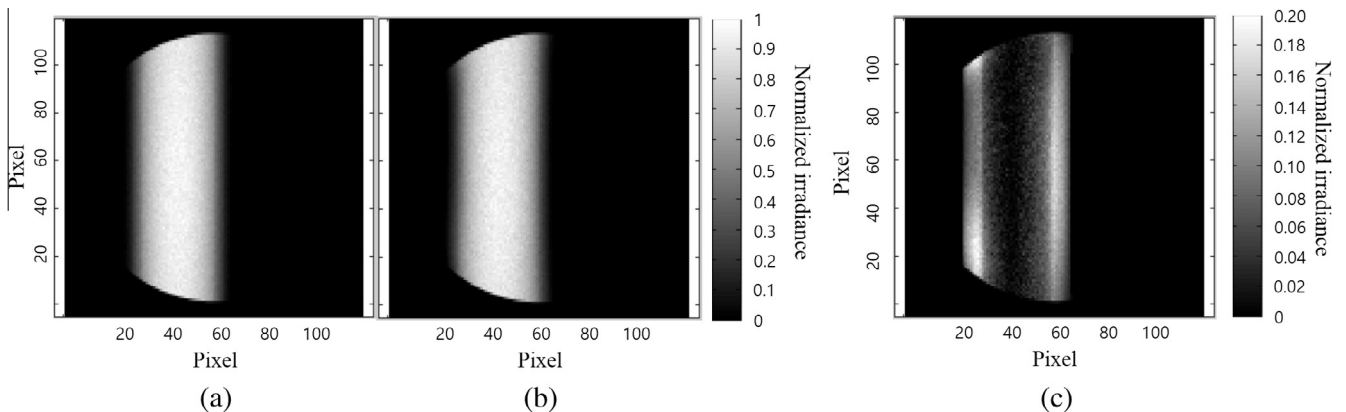

Fig. 3. Simulated mirror images. (a) Is a mirror image with one line illumination to the input spherical surface. (b) Is formed by the same light source as (a), but with the input surface with deviation. (c) Is a difference plot between (a) and (b). Color bar scale represents the normalized irradiance of each pixel.
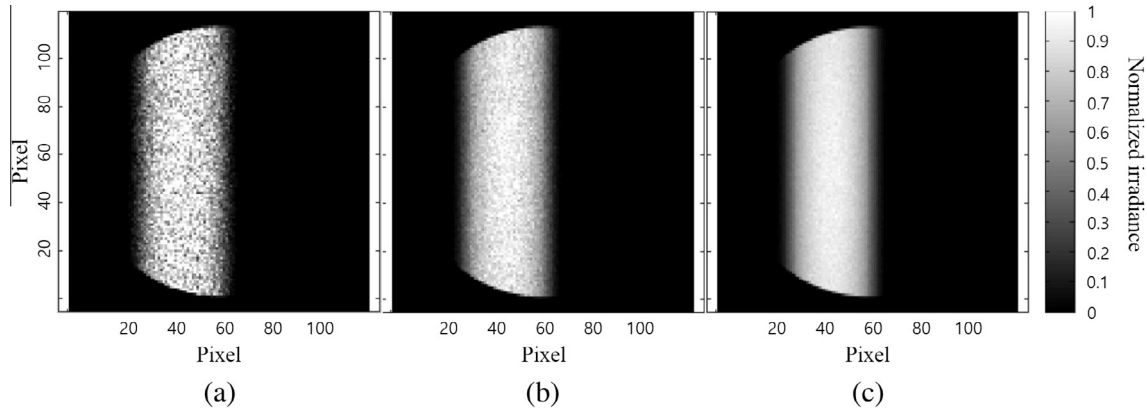
Fig. 4. Mirror images from specific line illumination with increasing ray number i.e. (a) 156,250 rays, (b) 1,562,500 rays, (c) 15,625,000 rays. Color bar scale represents the normalized irradiance of each pixel.

49.71 for 156,250 rays, 1,562,500 rays and 15,625,000 rays respectively.

Fig. 5 shows the light curves at the center pixel of the detector plane. "Coordinate of line" means the center of each screen line represented by the coordinate of global X axis. We note that the simulated irradiance vs line center coordinate follows the first order theoretical prediction very closely. We computed irradiances for all line images as appeared in Fig. 5. The theoretical light curve calculated from Eq. (2) appears as dotted line and the simulation results are expressed in symbols. We input 1 to r, L and Ω_p because they are constant in this case. A_w is defined as projected line area on the camera aperture when a line sweeps across the screen. Although Eq. (2) is derived from the first order approximation, it agrees very well with the simulation result. This is because the case is very similar to the condition used in Eq. (2). The difference between the two curves is 3.0%, 1.5% and 0.3% for 156,250 rays, 1,562,500 rays and 15,625,000 rays respectively. We note from Fig. 6 that the centroid values changes from 0.001 mm for the ideal spherical surface to 0.045 mm for the spherical surface with the added 0.4828 μm deviation.
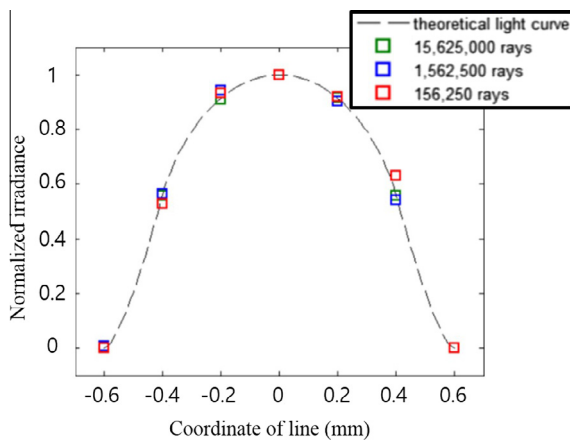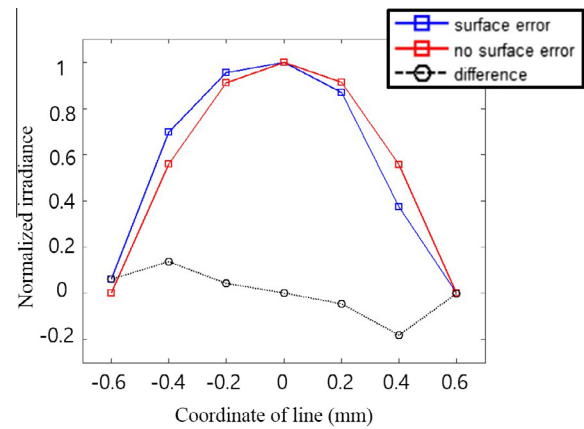

Fig. 6. Light curve profiles obtained at the detector center pixel with and without surface deviation (0.4828 μm rms).

3.2. Zonal surface reconstruction

The target surface is re-constructed from using Eqs. (3) and (4) and zonal estimation algorithm (Southwell, 1980). Fig. 7 shows reconstructed slope, surface height and surface deviation. The simulation quality is verified with the rms difference between the input surface data and reconstructed surface data from SCOTS simulation image analysis. Fig. 7(d) is the map of reconstructed surface deviation represented by Zernike polynomials in Table 4. Fig. 8 and Table 5 show the rms difference corresponding to each simulation case of ideal surface and surface deviation with different ray number. The rms difference depends heavily on the ray number, while the surface deviation does not affect simulation quality greatly. From these results, we understand that the use of more than 15 million rays is essential, should the reconstruct target surface is to achieve about 1 nm rms in height difference from the input surface.

The surface deviation can be represented by the combination of low order terms (6, 8, 9, 11) and high order terms (29, 38) of Zernike polynomials. Table 5 shows the input and output coefficients and their difference. The differences
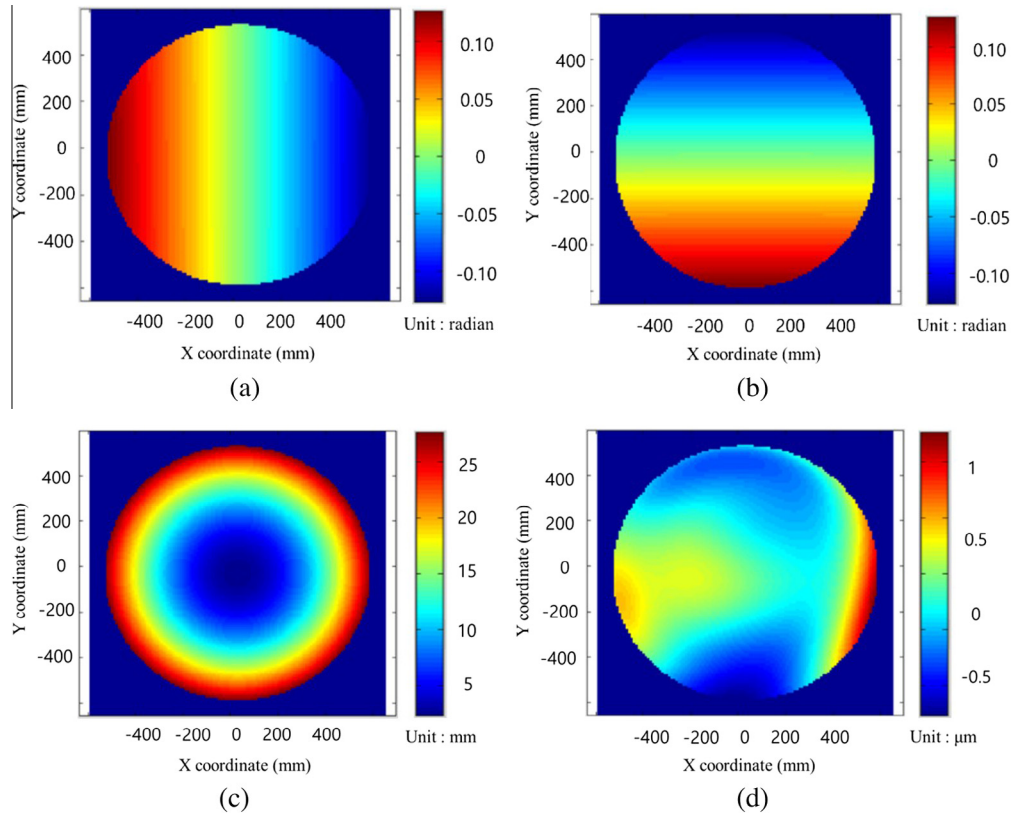

Fig. 5. Light curve data of line scanning from the simulation and theoretical calculation at the detector center pixel.

Fig. 7. Simulation result for spherical surface with deviation (0.4828 μm rms). Plot (a) and (b) show slopes in two orthogonal directions. The reconstructed surface height (c) and surface deviation (d) are shown.

Table 4
Zernike coefficients representing input and output surfaces, and their differences. Ray numbers used for the output data is 15,625,000.

Zernike term (order)	Input coefficient (μm)	Output coefficient (μm)	Difference (μm)
Primary Astigmatism x (6)	0.3266	0.3262	−0.0004
Primary Coma x (8)	−0.1414	−0.1408	0.0006
Primary Trifoil y (9)	0.1061	0.1059	−0.0002
Primary Spherical (11)	0.0894	0.0877	−0.0017
Tertiary Coma x (29)	−0.0250	−0.0247	0.0003
Quaterary Astigmatism y (38)	−0.0141	−0.0143	−0.0002
Rms surface deviation (μm)	0.4828	0.4827	−0.0001

between each input and output coefficient is 0.5 nm on average. The difference between the input and output surface deviations is only 0.1 nm rms and it is similar between low and high order term except for the 11th term. The difference on the 11th Zernike term is related to the error occurred at the edge of the surface because the number of neighboring data point are insufficient.

In the real SCOTS test, relatively high errors are occurred in low order Zernike terms (Su et al., 2014). This is mainly caused by uncertainty in measuring position of each components in SCOTS. IRT simulation can analyze the geometric uncertainty effects onto the surface test by simulating the pattern image variation due to the position variation in the model. However, we acknowledge that these geometric effects can be modeled and analyzed using

geometrical approaches such as ZEMAX sequential ray tracing models. The non-sequential IRT model will basically produce identical results as the geometrical methods, but will be less efficient in terms of numerical computing cost. (Note: The comparable optical simulation performance between sequential (e.g. CODE V and ZEMAX) and non-sequential (e.g. ASAP) ray tracing tools for geometrical analysis such as misalignment aberrations has been well investigated and demonstrated in various other studies (Cote and Tesar, 1998; Cote et al., 1999).) The unique advantage of IRT method, in fact, is that it can be used to evaluate the low order uncertainties caused by non trivial higher order effects. Although SCOTS deflectometry concept is purely based on geometric ray tracing calculations, the actual metrology results can be affected
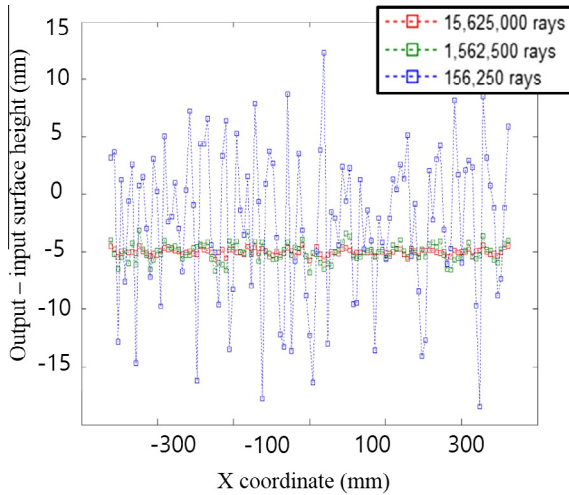
Fig. 8. Difference between input and reconstructed spherical surface heights.

by non-geometrical error sources such as radiometric uniformity of the line images on detector pixels. For instance, the detector efficiency, screen pixel brightness variation and scattering from the camera lens surface can cause a systematic false signal in the measured images producing low order Zernike term uncertainties. Three case studies considering non-geometric errors are summarized in the following Section 3.3.

3.3. Non-geometrical error source analysis

First, we estimated the effect of screen pixel brightness variation with the ideal spherical surface mentioned in the previous section. Fig. 9 shows the simulated screen pixel brightness variation distribution pattern with reconstructed surface difference from the no variation case. We used ±10 % variation in hypothetical input brightness changes. This represents the worst case linear and random disturbances to the screen's brightness uniformity. The IRT simulation and image data processing resulted in 94.09 nm (linear variation) and 43.01 nm (random variation) in the surface height difference between the ideal surfaces with and without brightness variations. We also observe a strong effect from low order Zernike terms in Fig. 9(c) as we discussed in Section 3.2. For these computations, the numerical error turned out to be about 7.08 nm rms with 156,250 rays used. These demonstrate that the SCOTS measurement can be affected significantly by the screen's

brightness variation pattern and the IRT computation is a useful tool to analyze it.

Second, for studying static scattering effect of the target mirror surface to the SCOTS measurement, we used Harvey scattering model with 0.25% TIS (Ellis and Pfistere, 2003). The TIS value is derived from the 2 nm in Ra (Roughness average) at 500 nm following the requirements of GMT FSM. The locations of scattered light rays falling onto the detector plane are not changed with time. As shown in Fig. 10, the scattered light tends to diverge to the detector plane. Then, the scattered irradiance tends to fall down to only 10^{-8} of the main line pattern image irradiance level. This corresponds to only 3.8×10^{-10} nm rms in surface height. Therefore, we see the negligible scattering effect to the SCOTS measurement results, if the target surface was well polished to 2 nm Ra and the scattered light received at the detector plane was not changed with time. However, in the shop floor measurement environment, the scattered light received by the detector can vary its location with time. This can be caused by vibration and air turbulence during the measurement exposure time. Such time varying scattering effect is beyond the scope of this study and the detailed study on the effects of time variation of scattered light is an important part of our future work scope.

3.4. Off-axis aspherical surface

Using the same ray tracing technique and surface reconstruction method, we also simulated SCOTS test for an off-axis aspherical surface. The surface shape is same as GMT FSM in Table 2. The camera and the screen are identical to those used for the spherical surface simulation. They are at 4378 mm in +Z distance from the target surface vertex and separated apart by 70 mm. In this test configuration, 303 by 359 screen pixels were used to form the target image. 1,562,500 rays were used to generate one screen pixel's illumination. Fig. 11 shows the simulated mirror images under the screen line illumination. We note that the imaged lines are bent and this is caused by the line pattern reflected from the off axis aspherical surface.

Simulated images are converted to the surface height following the same computation as for the spherical surface. Fig. 12 shows the reconstructed surface map and the difference from input ideal surface. The difference between the input test surface and the reconstructed surface is 10.74 nm rms and this proves the nanometer

Table 5
Rms difference in slope and height between ideal surface and deviated surface.

Case	Ideal spherical surface			Surface deviation (0.4828 μm rms)		
Component	Slope x (μrad)	Slope y (μrad)	Height (nm)	Slope x (μrad)	Slope y (μrad)	Height (nm)
156,250 rays	2.6812	2.8056	7.08	2.6735	2.7937	6.69
1,562,500 rays	0.8642	0.9149	2.28	0.8678	0.9058	2.32
15,625,000 rays	0.3861	0.4418	1.10	0.3586	0.4263	1.05

Note: for the numerical precision used in the ray tracing, the results are rounded to 2 decimal places.
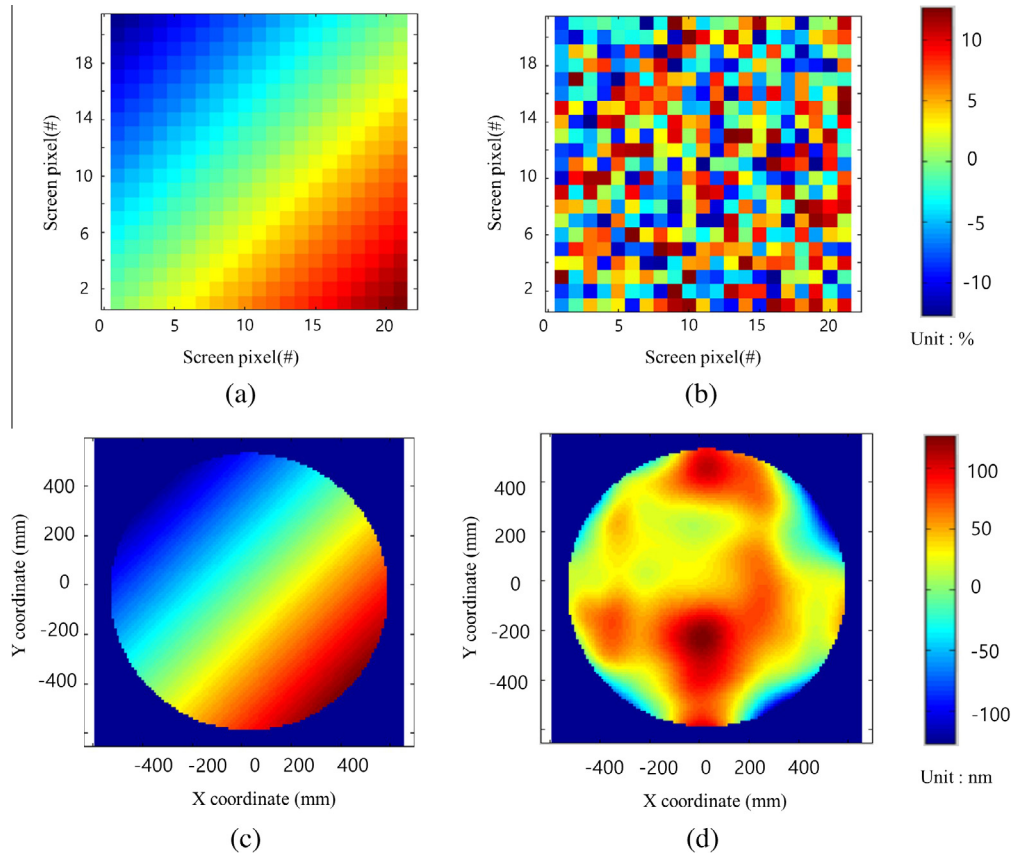
Fig. 9. IRT simulation results for screen pixel brightness variation. (a) and (b) Are for linear and random variation distributions respectively. (c) and (d) Are the 2D map representing height difference from the surfaces with and without the brightness variations.
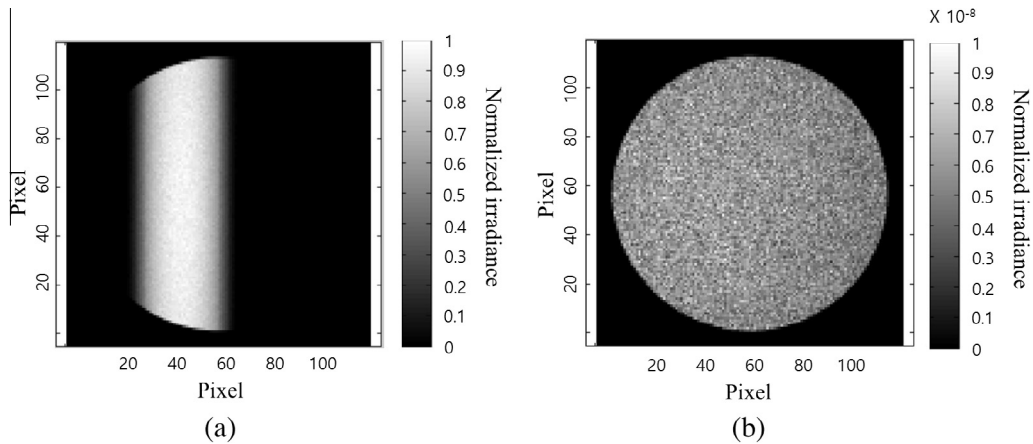

Fig. 10. (a) Is one of mirror images from specific line illumination and (b) is scattered light distribution map on the detector plane when the same screen pattern line is illuminated.

scale accuracy of the IRT SCOTS model performance in 1 m class aspheric mirror testing simulation.

4. Factor affecting simulation accuracy

First, the number of ray used tends to influence the simulation accuracy greatly. When the rays are emitted from the screen, the specific incident angle is randomly spread in order to simulate the screen illumination. This tends to generate the fluctuation within the simulated image as shown in Fig. 4. It would then cause slope and surface height error during the surface reconstruction. Regarding fluctuation from ray deficiency, the precision of centroid value σ_p can be estimated by using Eq. (5) (Butel et al., 2012). w is the width of light curve from the line scanning. N is the number of lines contributing to illumination of the
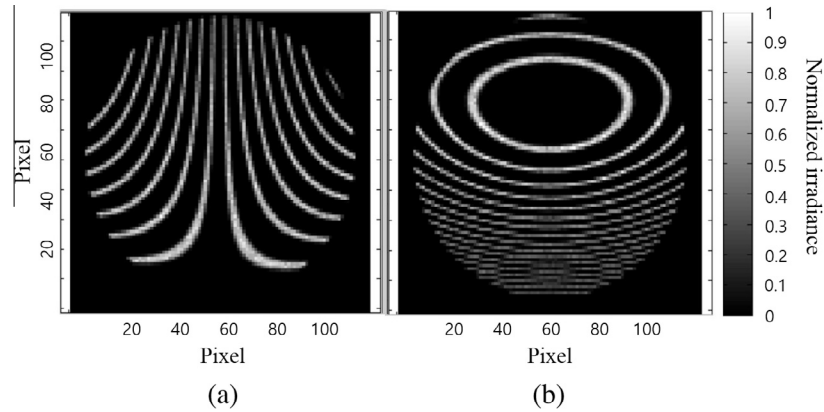
Fig. 11. Mirror images from illumination with 15 lines. (a) Is for X scanning direction and (b) is for Y scanning direction.
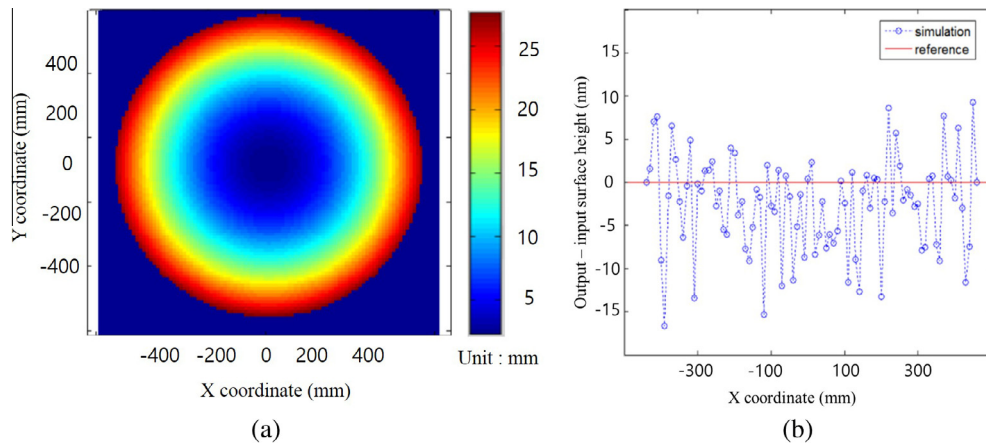

Fig. 12. (a) Is reconstructed surface height of off axis aspherical surface. (b) Is the plot of difference between input and reconstructed surface.

given detector pixel. SNR is the signal to noise ratio discussed in Section 3.1 and related to the irradiance fluctuation across the image.

$$\sigma_p = \frac{w}{2 \cdot \sqrt{N} \cdot \text{SNR}} \quad (5)$$

In the case of off-axis aspherical surface, the reconstruction error is five times higher than that of the spherical surface case with the same ray number, 1,562,500. The difference is caused by relative ray deficiency occurred in the case of off-axis aspheric surface. As aspheric departures is larger, rays entering the camera aperture is decreased. If we use ten times larger number of ray, about 5 nm rms reconstruction error can be obtained. The estimation is based on the relation of spherical surface's reconstruction error from the 1,562,500 rays and 15,625,000 rays cases. This implies that, for the surface fabrication requirement, 20 nm rms, it is feasible to use the IRT SCOTS simulation on the SCOTS test measurement of GMT FSM that is an off axis aspherical surface.

Second, the zonal estimation technique relies on the assumption of slope linearity across the radius. Therefore, the conversion error is inevitable, except for the paraboloid surface having linear slope. This error tends to decrease as the sampling points increases. In the case of 125 by 125 sampling points used in this study, the zonal estimation error is about 0.17 nm rms that is the tenth of the gross error from the case of 15,625,000 rays used.

Third, the ray tracing results at around the target surface edge tend to suffer from the insufficient number of neighboring data points. This leads to less accurate estimation of the centroid coordinate using Eq. (4) and hence larger location discrepancy from the light curve peak derived from using Eq. (2). These two locations should agree well, if a sufficient number of the neighboring data point were used.

Regarding the computation time, it takes 5 s for 156,250 rays per screen pixel with Intel Core i5 CPU running at 2.67 GHz. This leads to about 30 min in simulation time for 21 by 21 screen pixels. For 15,625,000 rays, it is extended to about 2 days in simulation time with the single core CPU and we note that it can be shortened proportionally if multi-core CPU was used. It is inevitable that running time is longer than existing analytic model because IRT model is based on the non-sequential ray tracing engine. However, IRT simulation can contribute to save

calibration efforts by performing in depth analysis for aforementioned error sources and provide the shop floor calibration with the useful guidelines, before the actual test starts.

5. Conclusion

For the first time, a non-sequential forward ray tracing simulation model of the SCOTS test method is constructed using the IRT technique and its computation performance was investigated. This new simulation model has sharp difference from the existing analytical tool (Su et al., 2015) that is a sequential reverse ray tracing computation. This new IRT SCOTS model is capable of performing both imaging and radiometric transfer computation simultaneously. And it can provide the SCOTS user with the test mirror image overlaid with the distorted fringe pattern that is the observable phenomena from the shop floor measurement.

We then used the IRT SCOTS test model for measurement simulation of the GMT FSM surface shape. After obtaining the target mirror image, the surface's slope and height were estimated. And using zonal estimation technique, the spherical target surface was reconstructed to 1 nm rms difference from the input surface height, provided that 15,625,000 rays was used in the ray tracing. It is also estimated that for the same ray number, about 5 nm rms difference would be occurred in the case of off axis aspherical surface.

We also demonstrated the capability of radiometric calculation in IRT simulation by analyzing numerical output of each detector pixel's irradiance. The case studies for linear and random brightness variations and for scattering effects were analyzed and the results demonstrate the usefulness of IRT computation in analyzing error sources influencing the SCOTS type measurement for large optical surfaces.

Comparing these results to other testing methods such as CMM and interferometry, this study shows the excellent potential that the PMD method tends to offer better measurement accuracy than that of CMM and comparable to that of interferometric testing method. Thus, PMD method would be a good cross verification tool to the interferometric testing method. The study also proves that the simulation performance quality falls within the GMT FSM surface fabrication requirement of 20 nm rms. It also implies that the simulation technique reported in this study would be very efficient and useful tool for the design and construction of SCOT type instrument for testing large precision surfaces including telescope mirrors. In future publications leveraging the newly developed IRT model, various final metrology data quality and performance will be investigated as a function of different error source variations using sensitivity analysis and Monte Carlo simulations. This statistical study would provide insights to develop more customized and efficient deflectometry systems.

References

Abdulkadyrov, M.A., Ignatov, A.N., Patrikeev, V.E., et al., 2004. M1 and M2 mirrors manufacturing for VISTA telescope. In: Proc. SPIE 5494, Optical Fabrication, Metrology, and Material Advancements for Telescopes, p. 374.

Breault, R.P., Kim, S.W., Yang, S.K., Ryu, D., 2014. Sun-, Earth- and Moon-integrated simulation ray tracing for observation from space using ASAP. In: Proc. SPIE 9189, Photonic Innovations and Solutions for Complex Environments and Systems (PISCES) II, 91890F.

Butel, G.P., Smith, G.A., Burge, J.H., 2012. Optimization of dynamic structured illumination for surface slope measurements. In: Proc. SPIE 8493, Interferometry XVI: Techniques and Analysis, 84930S.

Cho, M., Corredor, A., Cribusch, C., et al., 2014. Development of GMT fast steering secondary mirror assembly. In: SPIE Astronomical Telescopes+ Instrumentation. International Society for Optics and Photonics.

Comley, P., Morantz, P., Shore, P., Tonnellier, X., 2011. Grinding metre scale mirror segments for the E-ELT ground based telescope. CIRP Ann. 60 (1), 379–382.

Cote, M., Tesar, J.C., 1998. Optical system image irradiance simulations. In: Proc. SPIE 3482, International Optical Design Conference 1998, p. 397.

Cote, M., Pagano, R.J., Stevenson, M.A., 1999. Optical system performance visualization. In: Proc. SPIE 3780, Optical Design and Analysis Software, p. 2.

Davies, H., 1954. The reflection of electromagnetic waves from a rough surface. In: Proceedings of the IEE-Part IV: Institution Monographs 101.7, pp. 209–214.

Ellis, S., Pfistere, R.N., 2003. Advanced Technology Solar Telescope (ATST) Stray and Scattered Light Analysis.

Gallagher, B., Bergeland, M., Brown, B., et al., 2011. JWST mirror production status. In: Proc. SPIE 8146, UV/Optical/IR Space Telescopes and Instruments: Innovative Technologies and Concepts V, 814607.

Jeong, S., Jeong, Y., Ryu, D., 2009. In-orbit imaging and radiometric performance prediction for flight model Geostationary Ocean Color Imager. In: Proc. SPIE 7452, Earth Observing Systems XIV, 74520F.

Kiikka, C., Neal, D.R., Kincade, J., et al., 2006. The JWST infrared Scanning Shack Hartman System: a new in-process way to measure large mirrors during optical fabrication at Tinsley. In: Proc. SPIE 6265, Space Telescopes and Instrumentation I: Optical, Infrared, and Millimeter, 62653D.

Kim, Y.-S., Ahn, K.B., Park, K.J., Moon, I.K., Yang, H.S., 2009. Accuracy assessment for measuring surface figures of large aspheric mirrors. J. Opt. Soc. Korea 13, 178–183.

Kim, Y.S., Koh, J.H., Chung, I., et al., 2012. Development status of the prototype of the GMT fast steering mirror. In: 6th International Symposium on Advanced Optical Manufacturing and Testing Technologiesm, 84150B.

Knauer, M.C., Kaminski, J., Hausler, G., 2004. Phase measuring deflectometry: a new approach to measure specular free-form surfaces. In: Proc. SPIE 5457, Optical Metrology in Production Engineering, p. 366.

Lee, J.M., Park, W.H., Ham, S.J., et al., 2007. Integrated ray tracing model for end-to-end performance verification of Amon-Ra instrument. J. Astron. Space Sci. 24, 69–78.

Ligtenberg, F.K., 1954. The moire method, a new experimental method for the determination of moments in small slab models. Proc. SESA 12 (2), 83–98.

Martin, H.M., Zappellini, G.B., Cuerden, B., et al., 2006. Deformable secondary mirrors for the LBT adaptive optics system. In: Proc. SPIE 6272, Advances in Adaptive Optics II, 62720U.

Rodolfo, J., Chouarche, L., Chaussat, G., et al., 2012. Prototype segments polishing and testing for ELT M1. In: Proc. SPIE 8450, Modern Technologies in Space- and Ground-based Telescopes and Instrumentation II, 845023.

Ryu, D., Kim, S.W., Kim, D.W., et al., 2010. Integrated ray tracing simulation of annual variation of spectral bio-signatures from cloud free 3D optical Earth model. In: Proc. SPIE 7819, Instruments, Methods, and Missions for Astrobiology XIII, 78190E.

Seong, S., Kim, S.W., Ryu, D., Hong, J., Lockwood, M., 2012. Laboratory test simulation for non-flat response calibration of global Earth albedo monitor. In: Proc. SPIE 8533, Sensors, Systems, and Next-Generation Satellites XVI, 85331I.

Southwell, W.H., 1980. Wave-front estimation from wave-front slope measurements. J. Opt. Soc. Am. 70, 998–1006.

Su, P., Parks, R.E., Wang, L., et al., 2010. Software configurable optical test system: a computerized reverse Hartmann test. Appl. Opt. 49, 4404–4412.

Su, P., Oh, C.J., Zhao, C., Burge, J.H., 2012a. Optical testing for meter size aspheric optics. In: SPIE NanoScience+ Engineering International Society for Optics and Photonics, pp. 84660S–84660S.

Su, P., Wang, S., Khreishi, M., Wang, Y., et al., 2012b. SCOTS: a reverse Hartmann test with high dynamic range for Giant Magellan Telescope primary mirror segments. In: Proc. SPIE 8450, Modern Technologies in Space- and Ground-based Telescopes and Instrumentation II.

Su, P., Wang, Y., Burge, J.H., Kaznatcheev, K., Idir, M., 2012c. Non-null full field X-ray mirror metrology using SCOTS: a reflection deflectometry approach. Opt. Express 20 (11), 12393–12406.

Su, T., Wang, S., Parks, R.E., Su, P., Burge, J.H., 2013. Measuring rough optical surfaces using scanning long-wave optical test system. 1. Principle and implementation. Appl. Opt. 52, 7117–7126.

Su, P., Khreishi, M.A., Su, T., et al., 2014. Aspheric and freeform surfaces metrology with software configurable optical test system: a computerized reverse Hartmann test. Opt. Eng. 53 (3), 031305-031305.

Su, T., Maldonado, A., Su, P., Burge, J.H., 2015. Instrument transfer function of slope measuring deflectometry systems. Appl. Opt. 54 (10), 2981–2990.

Valente, M., Lewis, B., Melena, N., Smith, M., Burge, J. H., Zhao, C., 2013. Advanced surface metrology for meter-class optics. In: Proc. SPIE 8838, Optical Manufacturing and Testing X, 88380F.